Springer

KSME

Journal of Mechanical Science and Technology 32 (6) (2018) 2867~2875
www.springerlink.com/content/1738-494x(Print)/1976-3824(Online)
DOI 10.1007/s12206-018-0542-9

Self-adjusted adsorption strategy for an aircraft skin inspection robot †

Jiayue Gu*, Congqing Wang and Xuewei Wu

College of Automation Engineering, Nanjing University of Aeronautics and Astronautics, Nanjing 210016, China

(Manuscript Received June 27, 2017; Revised January 22, 2018; Accepted March 5, 2018)

Abstract

A self-adjusted adsorption strategy is developed for an aircraft skin inspection robot with double frames to improve adsorption safety and movement stability. The principal aim is to determine the optimal value of adsorption force when the robot slips or overturns on the fuselage. A pneumatic system that consists of suction cup and cylinder control is designed. Static force analysis shows that the adsorption force of the aircraft skin inspection robot is related to the curvature of the fuselage. The relationship between the minimum value of adsorption force and offset angle of the robot barycenter is established with the least-squares support vector regression algorithm. Pulse-width modulation is then applied to control the pressure difference in the suction cup. Experimental results prove the feasibility of suction cup control with the self-adjusted adsorption strategy.

Keywords: Aircraft skin inspection robot; Suction cup control; Static force analysis; Self-adjustment adsorption force

1. Introduction

To ensure that planes fly safely, people need to perform regular nondestructive testing of aircraft skin [1], but this procedure is difficult because it involves intense labor, long testing period, and high miss rates. In Refs. [2, 3], robots that use vacuum for adhesion and can crawl around the fuselage were introduced. An aircraft skin inspection robot has also been developed based on mobile climbing robots [4-8]. Climbing robots equipped with inspection devices can identify different damage types on the aircraft skin, including corrosion and fatigue crack [9].

As shown in Fig. 1, a double-frame structure is applied to the design of an aircraft skin inspection robot [10]. A digital signal processor (DSP) is used to control robot movement on the fuselage. The robot uses negative pressure adsorption, and eight suction cups are installed on the outer and inner frames. Therefore, the robot can adhere to the aircraft safely. The movements of the outer and inner frames are driven by stepping motors. The robot can move on the surface of the aircraft through the switching of the double frames. The front and rear double-acting cylinders elongate or shorten by different distances to change the posture of the robot.

If the adsorption force cannot be changed, the maximum adsorption force during the robot's climb along the fuselage must be maintained to ensure that the robot moves safely [11, 12]. Compared with constant adsorption [13], the changing adsorption in this work can improve movement stability [14]. The robot can adjust the adsorption force when the barycenter angle is changed to satisfy the minimum adsorption force.

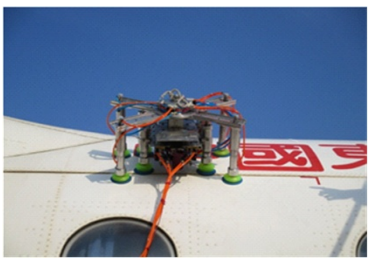

Fig. 1. Aircraft skin inspection robot with double frames.

The rest of this paper is structured as follows. Sec. 2 presents a static force analysis of a robot on a surface. Sec. 3 introduces the pneumatic system of an aircraft skin inspection robot. Sec. 4 presents a self-adjusted adsorption strategy, and Sec. 5 shows the analysis of experimental results. Sec. 6 provides the conclusions.

2. Analysis of optimal adsorption force

When an aircraft skin inspection robot moves on the surface of an aircraft, sufficient adsorption force must be guaranteed to avoid sliding and overturning. Static force analysis assumes that the aircraft fuselage is a cylindrical surface. An optimal-adsorption mechanical model was established in a previous study [15, 16] through an analysis of force balance to improve

*Corresponding author. Tel.: +86 15852925626
E-mail address: 15852925626@163.com
† Recommended by Associate Editor Joonbum Bae

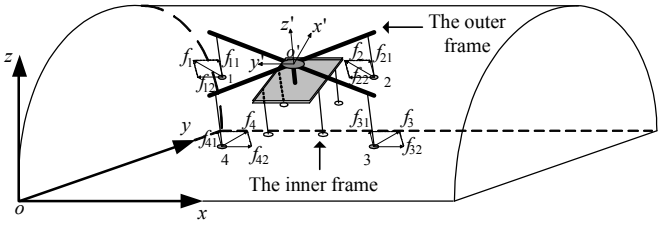

(a) Front view of a robot on a curved surface

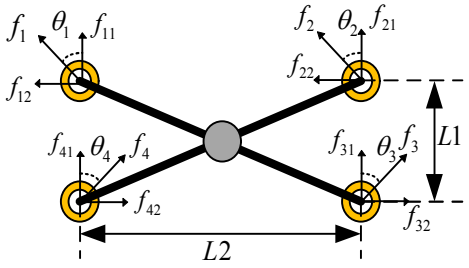

(b) Vertical view of a rob

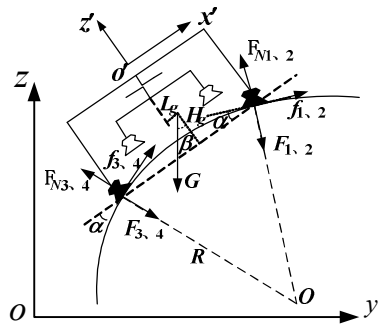

(c) Side elevation of a robot

Fig. 2. Static force analysis of a robot on a curved surface.

the stability of robot movements. Two cases were considered. The first one was anti-slipping state, in which the robot slid along the surface of the aircraft. The second case was anti-overturning state, in which the robot rolled around a line formed by two suckers. The specific force analysis is shown in Fig. 2.

In Fig. 2(a), $o-xyz$ is the global coordinate system, and $o'-x'y'z'$ is the coordinate system centrally located on the outer frame of the robot. $x'o'y'$ is parallel to the plane of the outer frame, and the suction cups installed on the outer frame are defined in a clockwise direction as numbers 1, 2, 3, and 4. f_i is the frictional force acting on the suction cup $i(i=1,2,3,4)$, and it is divided into f_{i1} and f_{i2} along the curved surface in the tangential direction. In Fig. 2(b), L_1 is the distance between the front and rear legs of the robot, L_2 is the distance between the left and right legs of the robot, and θ_i is the angle between the frictional force acting on the suction cup $i(i=1,2,3,4)$ and the tangent plane of the position of suction cup i. In Fig. 2(c), G is the gravity of the robot, F_i is the adsorption force resulting from the different pressures between the inside and outside of sucker i, F_{N_i} is the supporting force acting on the ith sucker, α is the dip angle caused by the deformation of a sucker, and β is the offset angle of the barycenter. L_g is the offset of the barycenter, H_g is the distance from the barycenter to the plane formed by four suckers, and R is the radius of fuselage curvature.

The equation of adsorption forces can be expressed as

$$F_1 = F_2 = F_3 = F_4 = \pi r^2 p\eta = F \ , \tag{1}$$

where r denotes the effective adsorption radius of the suction cup, η denotes the gas safety factor, and p denotes the difference between atmospheric pressure and the pressure in the suction cup.

The supporting forces arising from the different positions of $F_{N_{3,4}}$ and $F_{N_{1,2}}$ can be expressed as

$$\begin{aligned} &F_{N_{1,2}} \neq F_{N_{3,4}} \\ &F_{N_3} = F_{N_4} \\ &F_{N_1} = F_{N_2} \end{aligned} \ . \tag{2}$$

The frictional force on the ith suction cup can be expressed as

$$f_i = \mu F_{N_i} \ , \tag{3}$$

where μ is the friction coefficient.

2.1 Description of adsorption force balance

The equilibrium equations of adsorption forces and the torque equilibrium equations are expressed respectively as

$$\begin{cases} \sum_{i=1}^{4} f_i \cos\theta_i \cos\alpha + \sum_{i=3}^{4} F_i \sin\alpha - \sum_{i=1}^{2} F_i \sin\alpha + \sum_{i=1}^{2} F_{N_i} \sin\alpha \\ -\sum_{i=3}^{4} F_{N_i} \sin\alpha - G\sin\beta = 0 \\ \sum_{i=1}^{2} f_i \sin\theta_i - \sum_{i=3}^{4} f_i \sin\theta_i = 0 \\ \sum_{i=3}^{4} f_i \cos\theta_i \sin\alpha - \sum_{i=1}^{2} f_i \cos\theta_i \sin\alpha + \sum_{i=1}^{4} F_{N_i} \cos\alpha \\ -\sum_{i=1}^{4} F_i \cos\alpha - G\cos\beta = 0 \end{cases} , \tag{4}$$

$$\begin{cases} \sum_{i=1}^{4} f_i \sin\theta_i \frac{L_1}{2} - [f_1\cos\theta_1 - f_2\cos\theta_2 - f_3\cos\theta_3 - f_4\cos\theta_4]\cos\alpha\frac{L_2}{2} = 0 \\ \left(\sum_{i=1}^{2} f_i\cos\theta_i + \sum_{i=3}^{4} f_i\cos\theta_i\right)\sin\alpha\frac{L_1}{2} - \left(\sum_{i=1}^{2} f_i\cos\theta_i + \sum_{i=3}^{4} f_i\cos\theta_i\right)\cos\alpha H_g \\ -G\sin\beta H_g + G\cos\beta L_g + (2F_{N1} - 2F_{N3})\sin\alpha H_g + (2F_{N1} - 2F_{N3})\cos\alpha\frac{L_1}{2} = 0 \\ \left(-f_1\cos\theta_1 + f_2\cos\theta_2 - f_3\cos\theta_3 + f_4\cos\theta_4\right)\sin\alpha\frac{L_2}{2} = 0 \end{cases} \tag{5}$$

In accordance with the symmetric relation with the axis of the suction cup center, the torque equilibrium equations are expressed as

$$\begin{cases} -\sum_{i=3}^{4}(F_i - F_{N_i})\cos\alpha L_1 + \sum_{i=3}^{4} f_i\cos\theta_i\sin\alpha L_1 - \\ G\sin\beta H_g - G\cos\beta(\frac{L_1}{2} - L_g) = 0 \\ \sum_{i=1}^{2}(F_i - F_{N_i})\cos\alpha L_1 + \sum_{i=1}^{2} f_i\cos\theta_i\sin\alpha L_1 - \\ G\sin\beta H_g + G\cos\beta(L_g + \frac{L_1}{2}) = 0 \end{cases} \tag{6}$$

According to Eqs. (4)-(6), the balance equations of the supporting forces can be simplified as

$$\begin{cases} F_{N_1} = F_{N_2} = \dfrac{2F\cos\alpha L_1 + G\cos\beta(L_g + \frac{L_1}{2}) - G\sin\beta H_g}{2\cos\alpha L_1 - \mu\sin\alpha L_1(\cos\theta_1 + \cos\theta_2)} \\ F_{N_3} = F_{N_4} = \dfrac{2F\cos\alpha L_1 + G\cos\beta(\frac{L_1}{2} - L_g) + G\sin\beta H_g}{2\cos\alpha L_1 + \mu\sin\alpha L_1(\cos\theta_3 + \cos\theta_4)} \end{cases} \tag{7}$$

2.2 Anti-overturning and anti-slipping conditions

We assume that the robot does not slip, that is, $\theta_i = 0 (i = 1,2,3,4)$. The supporting forces are given by

$$\begin{aligned} F_{N_1} = F_{N_2} &= \frac{2F\cos\alpha L_1 + G\cos\beta(L_g + \frac{L_1}{2}) - G\sin\beta H_g}{2\cos\alpha L_1 - 2\mu\sin\alpha L_1} \\ F_{N_3} = F_{N_4} &= \frac{2F\cos\alpha L_1 + G\sin\beta H_g + G\cos\beta(\frac{L_1}{2} - L_g)}{2\cos\alpha L_1 + 2\mu\sin\alpha L_1} \end{aligned} \tag{8}$$

When the robot adheres to the surface of the aircraft skin, interaction forces arise between the suction cups and the surface of the aircraft. The critical overturning condition is $F_{N_1} = F_{N_2} = 0$. Therefore, the minimum anti-overturning adsorption force is expressed as

$$F_{q\min} = \frac{G\sin\beta H_g - G\cos\beta(L_g + \frac{L_1}{2})}{2\cos\alpha L_1}. \tag{9}$$

When the surface of the aircraft skin is very smooth, the adsorption forces are extremely small that the robot may slip from the aircraft. A critical condition when the robot begins slipping on the aircraft is that friction forces must offset the effect of robot gravity. The balance equation of supporting forces can be expressed as

$$2\mu(F_{N_1} + F_{N_3})\cos\alpha + 2(F_{N_1} - F_{N_3})\sin\alpha = G\sin\beta. \tag{10}$$

According to Eqs. (8) and (10), the minimum adsorption force of anti-slipping $F_{h\min}$ is expressed as

$$F_{h\min} = \frac{G\sigma}{4\mu\cos\alpha L_1}, \tag{11}$$

where

$$\begin{aligned} \sigma &= 2(\mu^2 + 1)\sin\alpha\cos\alpha\sin\beta H_g + \cos^2\alpha\sin\beta L_1 \\ &-2(\mu^2 + 1)\sin\alpha\cos\alpha\cos\beta L_g - \mu^2\sin^2\alpha\sin\beta L_1 - \mu\cos\beta L_1. \end{aligned}$$

The experimental parameters are set as follows: The robot with a weight of about 5 kg is selected as the object of the experiment, the coefficient of sliding friction μ is assumed to be 0.4, four suckers are installed on the inner frame of the robot, and the distance from the centroid of the suckers to the aircraft is 0.12 m. If the barycenter offset L_g is extremely small that the robot may slip or overturn, L_g can be set to 0.01 m. The fuselage curvature is assumed to be an invariant constant when obtaining the simulation data, and dip angle α of the suction cup is 5°, 10° and 15°. The curves of minimum adsorption force under anti-slipping and anti-overturning conditions are shown in Fig. 3.

The safety of mobile robots is associated with robot parameters (R and β). In Figs. 3(a) and (b), when dip angle α of the suction cup is 5°, 10° and 15°, the minimum anti-overturning and anti-slipping adsorption forces decrease with the increase in fuselage curvature. Under the same fuselage curvature R, the larger dip angle α is, the smaller the minimum anti-overturning and anti-slipping adsorption forces are.

In Fig. 3(c), if the range of the offset barycenter angle is $0^\circ - 27^\circ$, the robot can move on the fuselage with a small adsorption force. This situation conserves energy and enhances robot flexibility. The adsorption force should be equal to or greater than the minimum adsorption force of anti-slipping $F_{h\min}$ to enable the robot to move around the fuselage safely.

According to Eqs. (1) and (11), the equation of minimum adsorption force and robot barycenter angle can be simplified as

$$F = -\pi r^2 P_1 \eta = F_{h\min} = \frac{G\sigma}{4\mu\cos\alpha L_1}, \tag{12}$$

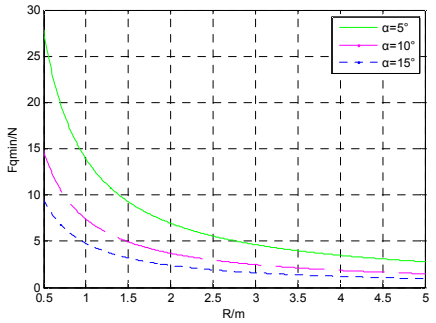

(a) Minimum anti-overturning adsorption forces vs. the radius of fuselage curvature

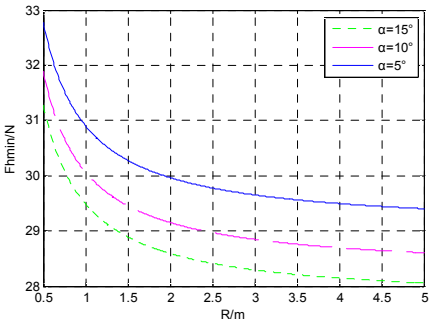

(b) Minimum anti-slipping adsorption forces vs. the radius of fuselage curvature

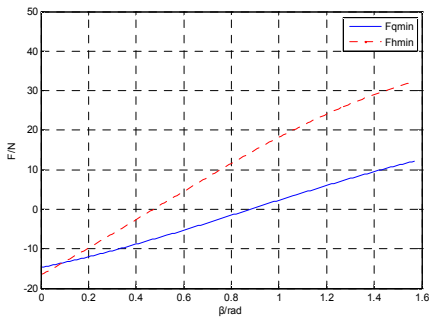

(c) Minimum adsorption forces vs. the fuselage curvature

Fig. 3. Curves of minimum adsorption force.

where P_1 denotes the difference between the pressure in the suction cup and atmospheric pressure.

3. Pneumatic system design

In Fig. 4, the configuration of the pneumatic system is divided into cylinder and suction cup control, and the air flow direction is indicated by an arrow. The action of suction cup control can change the adsorption force to enable the robot to move safely.

The suction cup is connected to port (2) of the three-way, high-frequency solenoid valve. The air source is connected to port (3) as the air inlet. The vacuum generator is connected to the port (1) as the air outlet. The startup and closing durations of the solenoid valve [17] can be controlled to allow for gas inflow or outflow. Hence, the expected value of air flow can

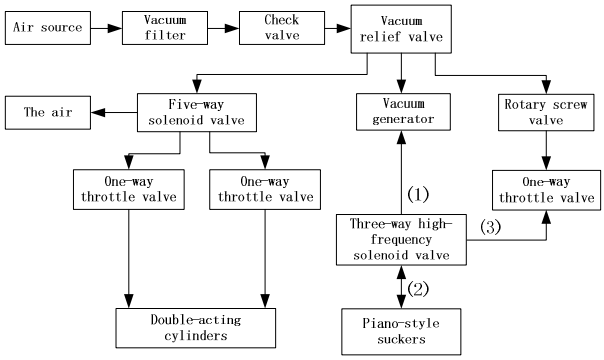

Fig. 4. Pneumatic system of the aircraft skin inspection robot.

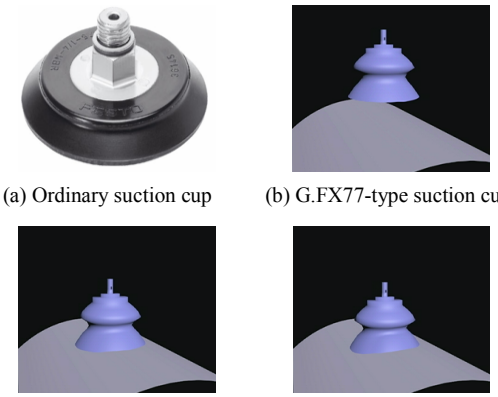

(a) Ordinary suction cup (b) G.FX77-type suction cup

(c) Beginning of adsorption (d) Adsorption of the suction cup

Fig. 5. Sucker adsorption process on the fuselage.

been obtained.

Fig. 5(a) shows an ordinary suction cup [18, 19], and Figs. 5(b)-(d) show a G.FX77-type suction cup. The structure of the G.FX77-type suction cup consists of an organ-type chamber and a seal lip. When this suction cup adheres to the aircraft, it can form an angle of 5°-30°. Therefore, the robot can adhere to the curved surface firmly. The sucker adsorption process is shown in Figs. 5(b)-(d).

4. Self-adjusted adsorption strategy

Under the control of the pulse-width modulation (PWM) signal, the opening and closing of the high-frequency solenoid valve make the times of air inflow and outflow [20] different. Therefore, obtaining an almost proportional flow rate is possible. The pulse-width signal is shown in Fig. 6, and its duty cycle is given by

$$d = \frac{T_{ON}}{T_C}, \tag{13}$$

where T_{ON} is the high-level duration of the PWM signal, T_C is the period of the PWM signal, d is the duty cycle of the PWM signal, and T_{Off} is the low-level duration of the PWM signal.

The self-adjusted adsorption force strategy is implemented

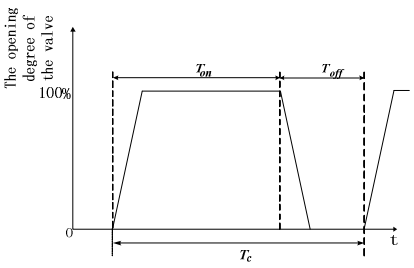

Fig. 6. Pulse-width modulation signal.

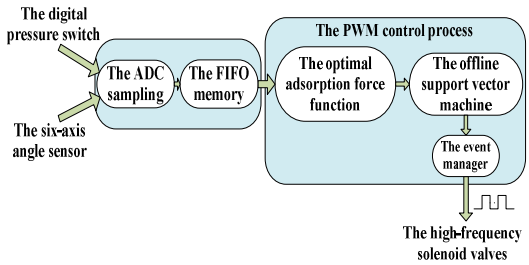

Fig. 7. Hardware implementation of the self-adjusted adsorption force strategy.

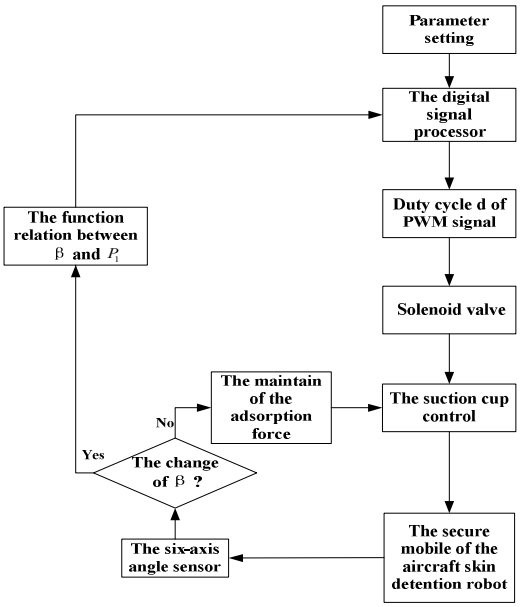

Fig. 8. Control procedure of adsorption self-adjustment.

with DSP, and the process is shown in Fig. 7. The value of pressure in the suction cup is obtained with a digital pressure meter. The six-axis angle sensor reveals the posture of the robot and sends this information to DSP. DSP then saves the sensor data in the FIFO memory. PWM control is implemented in the data processing module.

According to barycenter angle β of the robot, the duty cycle of the PWM signal is set by the DSP control board, as shown in Fig. 8. Thus, the value of air inflow or outflow in the suction cup is controlled by the solenoid valve. The maximum velocity of gas flowing into and out of the suction cup can be set as S_1 and S, respectively. If the duty cycle of the PWM wave is d, in unit time, the volume of air inflow will be $(1-d)S$ [21], and the volume of air outflow will be dS_1.

The gas-flow equations can be expressed as

$$\begin{aligned} Q_{in} &= -(1-d)P_1 S \\ Q_{out} &= -dP_1 S_1 \end{aligned}, \tag{14}$$

where P_1 denotes the difference between the pressure in the suction cup and atmospheric pressure.

Gas flow conservation [22] can be expressed as

$$Q_{in} - Q_{out} + Q_o = V\frac{dP_1}{dt}, \tag{15}$$

where Q_o is the air leakage of the suction cup in unit time, Q_{in} denotes the air inflow of the suction cup in unit time, Q_{out} is the air output of the suction cup in unit time, and V denotes the volume of the suction cup.

Designing a nonlinear controller with the least-squares support vector regression (LSSVR) algorithm is appropriate for the self-adjusted adsorption strategy due to the nonlinear relationship between the suction cup pressure difference and the duty cycle of the pulse-width modulation signal [23-25].

The LSSVR algorithm is used to establish a mathematical model between the pulse-width modulation duty cycle and the suction cup pressure difference. The process is described as follows.

The training set is $\{x_i, y_i\}$ $(i = 1,2,3,\cdots,n), x_i \in R^n, y_i \in R$, where x_i denotes the pressure difference in the suction cup, y_i is the duty cycle of the pulse-width modulation signal, and n denotes the number of samples.

In the feature space, the regression function can be expressed as

$$f(x) = w^T \varphi(x) + b, \tag{16}$$

where $\varphi(x)$ denotes the kernel space mapping function, $w \in R^n$ denotes the weight vector, and b denotes the offset.

The LSSVR algorithm is used to solve the following optimal problem.

$$\begin{cases} \min J(w,\varepsilon) = 0.5 \| w \|^2 + \dfrac{C}{2}\sum_{k=1}^{n} \varepsilon_k^{\,2} \\ s.t. \quad y_i = w^T \varphi(x_k) + b + \varepsilon_k, \ k = 1,2\cdots n \end{cases}, \tag{17}$$

where J denotes the optimization objective function, $\varepsilon_k \in R$ denotes the relaxation factor, and $C \in R$ denotes the penalty factor.

The Lagrangian function can be expressed as

$$L = J(w,\varepsilon) - \sum_{i=1}^{n}[a_i(w^T \varphi(x_i) + b + \varepsilon_i - y_i)], \tag{18}$$

where $a_i (i = 1, 2, ...n)$ is a Lagrange multiplier.

On the basis of Karush–Kuhn–Tucker (KKT) conditions, the optimal solution of Eq. (18) can be given as

$$w = \sum_{i=1}^{n} a_i \varphi(x_i) \, , \; a_i = C\varepsilon_k \, , \; \sum_{i=1}^{n} a_i = 0 \, , \; w^T \varphi(x_i) + b + \varepsilon_i = y_i \, .$$

To improve accuracy and computational efficiency, the Gaussian radial basis function is defined as

$$K(x_i, x_j) = \exp(-\gamma \| x_i - x_j \|^2) \, , \tag{19}$$

where γ is the width parameter, which controls the radial range of the function.

The prediction function can be expressed as

$$f(x) = \sum_{i=1}^{n} a_i K(x_i, x) + b \, . \tag{20}$$

The mean square error (MSE) is used to measure the accuracy of the mathematical model, and it can be expressed as

$$MSE = \frac{1}{n} \sum_{i=1}^{n} (y_i - f(x_i))^2 \, , \tag{21}$$

where n is the number of training samples (predicting samples), y_i is the actual output value of training samples (predicting samples) for the duty cycle of the PWM signal, and $f(x_i)$ is the LSSVR output value of training samples (predicting samples).

5. Analysis of experimental results

Experiments with different duty cycles were conducted on suction cup control. A suction cup (Piab.FX77), a rotor flowmeter, and three pairs of digital pressure switches used. The diameter of the suction cup was 77 mm. The values of air inflow and air output were set as 5 and 12 L/min, respectively. The sampling period of DSP was set as 16 ms. The adsorption process is shown in Fig. 9, where the y-axis is the pressure difference $p1$. When duty cycle d was 30 %, 55 %, 60 % and 70 %, the pressure equilibrium value differed. Thus, the self-adjusted adsorption control can be applied to the robot.

As shown in Fig. 10, self-adjusted adsorption control was applied to the aircraft skin inspection robot when the pressure difference in the suction cup was −6.5, −13, −14.3 and −17 KPa. The sucker deformations are shown in Fig. 10.

The LSSVR algorithm was used with the experimental data to establish a mathematical model for the relation between the duty cycle of the PWM signal and the suction cup pressure difference. The suction cup pressure difference was the input value of the LSSVR model, and the duty cycle of the PWM signal was the output value. The sample data were divided into nine sets of training samples and six sets of predicting samples. The value of duty cycle d and pressure difference

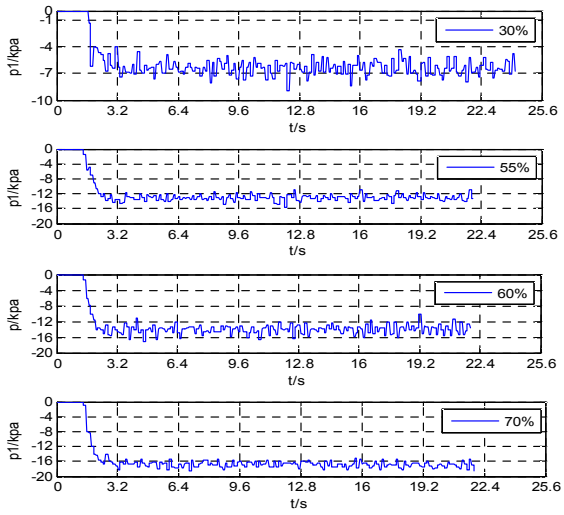

Fig. 9. Adsorption process in different duty cycles.

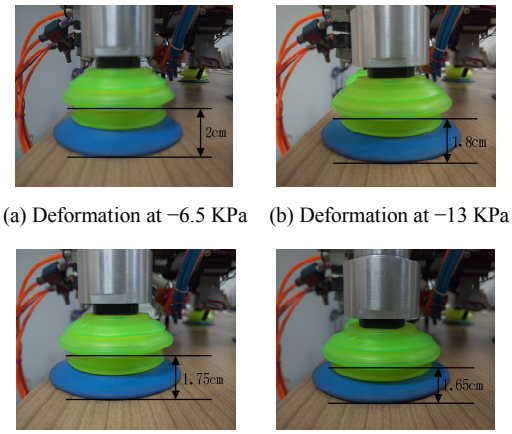

(a) Deformation at −6.5 KPa (b) Deformation at −13 KPa

(c) Deformation at −14.3 KPa (d) Deformation at −17 KPa

Fig. 10. Sucker deformation at different pressures.

p were normalized to [0, 1] and [−1, 0], respectively. In terms of cross validation, penalty factor C was determined to be 1, and γ=2.8 . The training result is shown in Fig. 11, in which the x-axis is pressure difference p , and the y-axis is the value of duty cycle d . The MSE of the training samples is 0.0413 %, and the MSE of the predicting samples is 0.068 %. The MSEs of the training and predicting samples are small, so the LSSVR model can be used to control the suction cup to stably adsorb or release.

This suction cup control was applied to the aircraft skin inspection robot. When offset angle β of the robot barycenter changed, adsorption force F was adjusted to satisfy the need to move and work on the surface of the aircraft. An arc-shaped aluminum plate was used as the surface of aircraft, and the received data on pressure in the suction cup were stored in the memory of DSP. Owing to the relational expression of differential pressure and adsorption force, the pressure was converted into adsorption force. The actual change in adsorption force and the simulation curves are shown in Fig. 12, in which

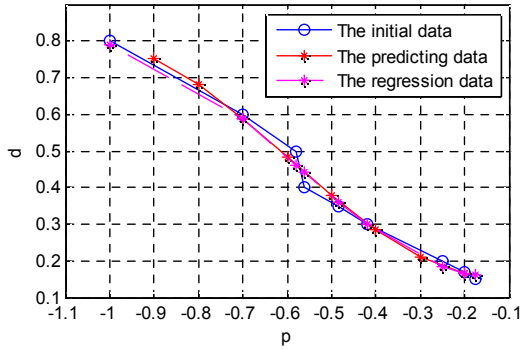

Fig. 11. Predicted result.

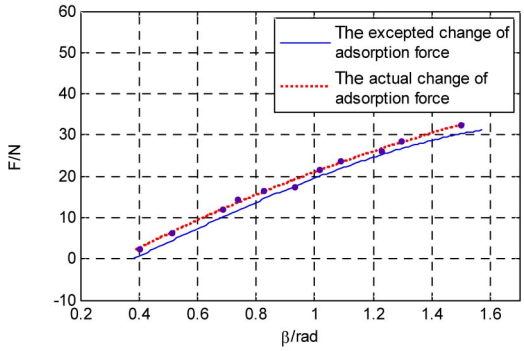

Fig. 12. Test and simulation curves.

the x-axis is offset angle β, and the y-axis is adsorption force F.

According to the self-adjusted adsorption control, the change curves of pressure difference $p1$ in the suction cup when the aircraft skin inspection robot moves from $\beta = 40°$ to $\beta = 60°$ or from $\beta = 64°$ to $\beta = 85°$ are shown in Fig. 13. When the suction cup adheres to the fuselage completely, the range of the pressure difference is ± 1.5 KPa, and the robot can stably move on the aircraft.

As shown in Fig. 14, the aircraft skin inspection robot with double frames releases the suction cups of the outer frame to move on the fuselage.

As shown in Fig. 9, the adsorption time of the suction cup was approximately 1.6 s, and with the increase in the duty cycle, the difference in pressure decreased evidently. Therefore, the LSSVR algorithm can be applied to establish a mathematical model effectively. When the pressure difference in the suction cup was constant, the actual value of the adsorption force was larger than the minimum adsorption force $F_{h\min}$ in the same barycenter angle (Fig. 12). Hence, the robot could work safely. The adsorption force could be adjusted with the change in the robot barycenter angle (Fig. 13), and the release time of the suction cup was shortened. As shown in Fig. 14, the aircraft skin inspection robot could move on the fuselage stably with the use of the designed pneumatic system. The experimental results verified the effectiveness of the adsorption force control strategy for the aircraft skin inspection robot.

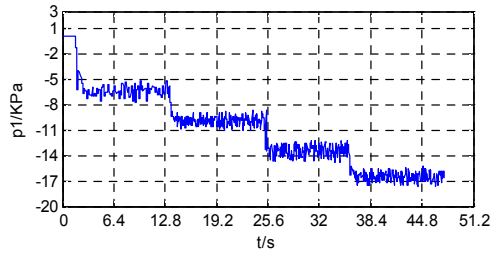

(a) Pressure changes from $\beta = 40$ to β=60°

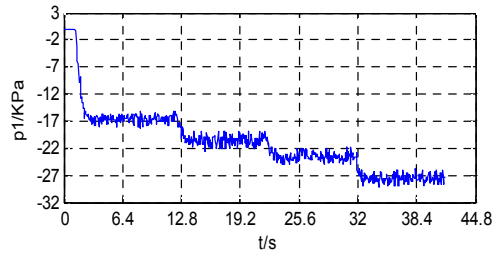

(b) Pressure changes from $\beta = 64°$ to $\beta = 85°$

Fig. 13. Changes in pressure difference in the sucker.

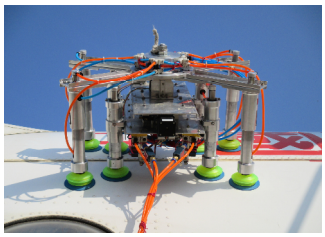

(a) Adsorption of the robot on the fuselage

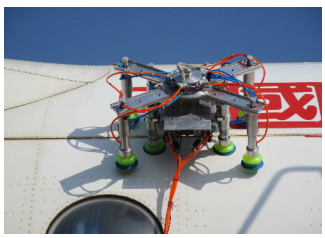

(b) Release of suction cups on the outer frame

Fig. 14. Movement of the aircraft skin inspection robot on the fuselage.

6. Conclusions

A self-adjusted adsorption strategy was designed in this work to resolve the problem of adsorption stability of an aircraft skin inspection robot on the surface of an aircraft. When the robot moved on the fuselage, the offset angle range of the robot barycenter was from $\beta = 40°$ to $\beta = 60°$ or from $\beta = 64°$ to $\beta = 85°$. The adsorption force could be adjusted to improve the flexibility of robot movement. Performance analysis of the pneumatic system showed satisfactory results on the adsorption stability of the robot with the self-adjusted adsorption strategy, which could reduce the jitter of the robot. The stable movement allowed the robot to easily adapt to the curvature of the fuselage.

The optimal adsorption condition of the aircraft skin inspection robot was determined based on a simulation analysis of a static model. The actual change in adsorption force with different offset angles was examined. The experimental results indicated that the actual adsorption force was greater than or equal to the optimal adsorption force, which could ensure that the robot moved safely on the aircraft. Therefore, the self-adjusted adsorption strategy can be applied to aircraft skin inspection robots.

Acknowledgments

This work was supported by the National Natural Science Foundation of China (Grant No. 61573185) and JiangSu Scientific Support Program of China (Grant No. BE2010190).

References

[1] J. Sanz, M. Ferre, A. Espada, M. C. Narocki and J. F. Pardo, Robotized inspection system of the external aircraft fuselage based on ultrasound, *The 2010 IEEE/RSJ International Conference on Intelligent Robots and Systems*, 2010 (2010) 2612-2617.

[2] G. Callow, J. Sargent, R. Alwxander, S. Cooke, S. Harris and T. S. White, A mobile climbing robot for high precision manufacture and inspection of aerostructures, *International Journal of Robotics Research*, 24 (7) (2005) 589-598.

[3] B. Bridge, J. Shang, S. Chen and T. Sattar, Design of a climbing robot for inspecting aircraft wings and fuselage, *Industrial Robot: An International Journal*, 34 (6) (2007) 495-502.

[4] M. A. Dean and D. D. Girish, Design, fabrication and testing of a smart robotic foot, *Robotics and Autonomous Systems*, 51 (2) (2005) 207-214.

[5] B. Bahr, Y. Li and M. Najafi, Design and suction cup analysis of a wall climbing robot, *Computers & Electrical Engineering*, 22 (3) (1996) 193-209.

[6] D. Kim, D. Chang, H. Yang, H. Kim, J. Kim, K. Seo and K. Lee, Development of a wall-climbing robot using a tracked wheel mechanism, *Journal of Mechanical Science and Technology*, 22 (8) (2008) 1490-1498.

[7] V. G. Loc, I. M. Koo, T. D. Trong, Y. K. Song, H. M. Kim, H. P. Moon and H. R. Choi, Sensing and control of quadruped walking and climbing robot over complex environment, *Proceedings of 2008 IEEE/RSJ International Conference on Intelligent Robots and Systems* (2008) 3884-3889.

[8] C. Schlosser and T. Schüppstuhl, Numerical controlled robot crawler: New resource for industries with large scale products, *Production Engineering*, 8 (6) (2014) 719-725.

[9] B. Joffe, P. G. Backes and B.-C. Yoseph, The multifunction automated crawling system (MACS), *Proceedings of SPIE-The International Society for Optical Engineering*, 1 (1) (1997) 335-340.

[10] C. Wang, X. Wang, X. Zhou and Z. Li, The aircraft skin crack inspection based on different-source sensors and support vector machines, *Journal of Nondestructive Evaluation*, 35 (3) (2016) 46.

[11] D. Sun, S.-K. Tso and J. Zhu, Development of a tracked climbing robot, *Journal of Intelligent and Robotic Systems*, 35 (4) (2002) 427-443.

[12] C. Cai, Y. Guan, L. Jiang, W. Wu, H. Zhang, L. Zhang, X. Zhou and H. Zhu, A modular biped wall-climbing robot with high mobility and manipulating function, *IEEE/ASME Transactions on Mechatronics*, 18 (6) (2013) 1787-1798.

[13] Y. Gong, X. Wang, Z. Wang and Z. Yi, A study on ultra-high pressure water jet wall climbing robot for removal rust in vessels, *Proceedings of the JFPS International Symposium on Fluid Power*, 2008 (7-2) (2008) 403-406.

[14] Y. Gong, X. Wang, Z. Wang and Z. Yi, Development of a wall climbing robot for ship rust removal, *International Conference on Mechatronics and Automation* (2009) 4610-4615.

[15] M. H. Pishrobat and J. Keighobadi, Robust output regulation of a triaxial MEMS gyroscope via nonlinear active disturbance rejection, *International Journal of Robust and Nonlinear Control*, 28 (8) (2017) 1-22.

[16] M. H. Pishrobat and J. Keighobadi, Force-balancing model predictive control of MEMS vibratory gyroscope sensor, *Proceedings of the Institution of Mechanical Engineers*, 230 (17) (2016) 3055-3065.

[17] J. Chen, H. Guan, Q. Wang, F. Yang and Q. Yang, Experimental analysis of new high-speed powerful digital solenoid valves, *Energy Conversion and Management*, 52 (5) (2011) 2309-2313.

[18] D. Ge, T. Matsuno, Y. Sun, C. Ren, Y. Tang and S. Ma, Quantitative study on the attachment and detachment of a passive suction cup, *Vacuum*, 116 (1) (2015) 13-20.

[19] J. Liu, K. Tanaka, L. M. Bao and I. Yamaura, Analytical modelling of suction cups used for window-cleaning robots, *Vacuum*, 80 (6) (2006) 593-598.

[20] G. M. Bone and R. B. van Varseveld, Accurate position control of a pneumatic actuator using on/off solenoid valves, *IEEE/ASME Transactions on Mechatronics*, 2 (3) (1997) 195-204.

[21] K. Ahn and S. Yokota, Intelligent switch -ing control of pneumatic actuator using on/off solenoid valves, *Mechatronics*, 15 (6) (2005) 683-702.

[22] N. Herakovic and M. Pipan, Volume flow character -ization of PWM-controlled fast-switching pneumatic valves, *Strojniski vestnik-Journal of Mechanical Engineering*, 62 (9) (2016) 543-550.

[23] J. Keighobadi, M. B. Menhaj and M. Kabganian, Feedback-linearization and fuzzy controllers for trajectory tracking of wheeled mobile robots, *Kybernetes the International Journal of Systems and Cybernetics*, 39 (1) (2010) 83-106.

[24] J. Keighobadi and M. B. Menhaj, From nonlinear to fuzzy approaches in trajectory tracking control of wheeled mobile robots, *Asian Journal of Control*, 14 (4) (2012) 960-973.

[25] M. R. Azizi and J. Keighobadi, Point stabilization of non-holonomic spherical mobile robot using nonlinear model predictive control, *Robotics and Autonomous Systems*, 98 (2017) 347-359.

Jiayue Gu is a Master's student in the College of Automation Engineering, Nanjing University of Aeronautics and Astronautics. His research interests include robot motion control, nonlinear control, and adaptive control.

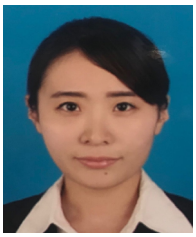

Xuewei Wu is a Ph.D. candidate in the College of Automation Engineering, Nanjing University of Aeronautics and Astronautics. Her research interests include robot motion control, switched systems, and nonlinear control.

Congqing Wang received his Ph.D. degree from Beijing University of Science and Technology in 1995. He is a Professor in the College of Automation Engineering, Nanjing University of Aeronautics and Astronautics. His research interests are in the areas of robotics, pattern recognition, and intelligent control.